PSFC/JA-10-16

I-Mode: An H-Mode Energy Confinement Regime with L-Mode Particle Transport in Alcator C-Mod.

D.G. Whyte

June 2010

Plasma Science and Fusion Center
Massachusetts Institute of Technology
Cambridge MA 02139 USA

This work was supported by the U.S. Department of Energy, Grant No. DE-FC02-99ER54512-CMOD.

I-mode: An H-mode Energy Confinement Regime with L-mode Particle Transport in Alcator C-Mod

D.G. Whyte, A.E. Hubbard, J.W. Hughes, B. Lipschultz, J.E. Rice, E.S. Marmar, M. Greenwald, I. Cziegler, A. Dominguez, T. Golfinopoulos, N. Howard, L. Lin, R.M. McDermott[1], M. Porkolab, M.L. Reinke, J. Terry, N. Tsujii, S. Wolfe, S. Wukitch, Y. Lin and the Alcator C-Mod Team
MIT Plasma Science and Fusion Center, Cambridge MA 02139 USA
Corresponding author: whyte@psfc.mit.edu
[1] *Present address: Max Planck Inst. for Plasma Physics, Garching, Germany*

An improved energy confinement regime, I-mode is studied in Alcator C-Mod, a compact high-field divertor tokamak using Ion Cyclotron Range of Frequencies (ICRF) auxiliary heating. I-mode features an edge energy transport barrier without an accompanying particle barrier, leading to several performance benefits. H-mode energy confinement is obtained without core impurity accumulation, resulting in reduced impurity radiation with a high-Z metal wall and ICRF heating. I-mode has a stationary temperature pedestal with Edge Localized Modes (ELMs) typically absent, while plasma density is controlled using divertor cryopumping. I-mode is a confinement regime that appears distinct from both L-mode and H-mode, combining the most favorable elements of both. The I-mode regime is obtained predominately with ion ∇B drift away from the active X-point. The transition from L-mode to I-mode is primarily identified by the formation of a high temperature edge pedestal, while the edge density profile remains nearly identical to L-mode. Laser blowoff injection shows that I-mode core impurity confinement times are nearly identical with those in L-mode, despite the enhanced energy confinement. In addition a weakly coherent edge MHD mode is apparent at high frequency ~ 100-300 kHz which appears to increase particle transport in the edge. The I-mode regime has been obtained over a wide parameter space (B=3-6 T, I_p=0.7-1.3 MA, q_{95}=2.5-5). In general the I-mode exhibits the strongest edge T pedestal and normalized energy confinement (H_{98}>1) at low q_{95} (<3.5) and high heating power (P_{heat} > 4 MW). I-mode significantly expands the operational space of ELM-free, stationary pedestals in C-Mod to T_{ped}~1 keV and low collisionality ν^*_{ped}~0.1, as compared to EDA H-mode with T_{ped}< 0.6 keV, ν^*_{ped}>1. The I-mode global energy confinement has a relatively weak degradation with heating power; $W_{th} \sim I_p P_{heat}^{0.7}$ leading to increasing H_{98} with heating power.

1. Introduction

Optimized magnetic fusion energy (MFE) reactors face the seemingly contradictory requirements of high global energy confinement and low particle confinement. In order to produce net energy gain, a minimum level of confinement parameterized by $n\tau_e \sim 10^{21}$ m^{-3} s [1] is required. Primarily due to the degradation of energy confinement time (τ_E) with heating power, it is generally acknowledged that the confinement quality factor, H, must at least attain values equal to "H-mode" high-energy confinement regimes in dominantly self-heated MFE reactors at reasonable size (see for example [2] [3]). However high global particle confinement time (τ_p) is not necessarily required since, unlike self-heating from alphas, the fuelling rate determining plasma density n is externally controlled. Simultaneously, overly high τ_p is usually undesirable due to the deleterious effects on fusion gain from accumulation of helium ash and impurity particles generated from plasma-wall interaction. Also, these global confinement times are largely set by the edge pedestal [4, 5], where an additional constraint is avoidance of peeling-ballooning instabilities which lead to MHD edge-localized modes (ELMs [6]) and unacceptable transient heating of plasma-facing components [7]. In general therefore one desires *independent* understanding and control of the energy and particle transport channels in the core and pedestal regions in order to optimize MFE scenarios.

We describe an improved energy confinement regime, I-mode, on Alcator C-Mod [8]. I-mode simultaneously features the desired properties of high-energy confinement of H-mode and the relatively poor particle confinement of low-confinement L-mode. The improved energy confinement results from the formation of an edge temperature pedestal, while density edge profiles remain essentially identical to those in L-mode. I-mode is most readily observed on C-Mod with the ion ∇B drift pointed away from the primary X-point, i.e. in the "unfavorable" configuration for obtaining H-mode from the power threshold standpoint. The pedestal is typically free of intermittent large ELMs yet plasma density is stationary, probably due to a high-frequency weakly coherent fluctuation contemporaneous with I-mode and observed in the pedestal region. I-mode demonstrates

that the energy and particle transport channels in the pedestal can be separated and isolated.

Previously, an "improved L-mode" regime was found and briefly described in ASDEX-Upgrade [9], which focused on the mode as an intermediate step in the transition to H-mode in the unfavorable ∇B configuration. Similar transient increases of edge electron temperature [10] and improved L-mode energy confinement [5] have been reported on C-Mod. Threshold studies on these tokamaks, as well as DIII-D, showed clearly that edge temperatures, T gradients and required heating power are substantially higher at the L-H transition in the unfavorable vs. favorable ∇B configuration [11-14]. More recently Alcator C-Mod [15] showed that the same enhanced confinement regime, labeled for the first time as "improved mode" or I-mode, could be made stationary. Charge-exchange recombination spectroscopy was used to show that I-mode pedestal had a radial electric field well structure similar to that of H-mode. (It should be noted that the I-mode described here and in [15] for *diverted* tokamaks should not be confused with the I-mode reported on the TEXTOR *limiter* tokamak [16] which does not feature an edge transport barrier).

We significantly expand on these previous I-mode studies by reporting on an extensive experimental campaign on Alcator C-Mod (Sec. 2). The study has the dual goals of 1) assessing the phenomenology of I-mode, and 2) extending operational experience, particularly towards achieving stationary I-mode discharges. The experimental results are organized as follows: identification of the distinguishing features of I-mode (Sec. 3.1), exploration of the parameter space which provides access to I-mode (Sec. 3.2), characterization of the global energy and particle confinement of I-mode (Sec. 3.3), and documentation of the edge pedestal and fluctuation characteristics of I-mode (Secs. 3.4-3.5). Sec. 4 discusses the C-Mod experimental results on I-mode and conclusions are presented in Sec. 5.

2. Experimental Setup

Experiments were carried out on the compact, high-field Alcator C-Mod divertor tokamak [8]: major radius R~0.67 m, minor radius a~0.22 and toroidal field B < 8 T. Unique among divertor tokamaks, C-Mod uses only high-Z bulk refractory metals of molybdenum and tungsten for plasma-facing components. Ion Cyclotron Range of Frequencies (ICRF) heating is the sole auxiliary heating method used in these experiments [17]. Fundamental hydrogen (H)-minority ICRF at 78-80.5 MHz up to 5.5 MW is used for central heating of deuterium (D) majority plasmas at typical magnetic field B ~ 5.4. For the purposes of this study, and consistent with previous reports [5], 80% absorption efficiency is assumed for fundamental H-minority heating. In addition, the study includes a campaign at reduced B field (~3-3.4 T) which primarily uses central ICRF H-minority 50 MHz heating, and some additional 80 MHz 2^{nd} harmonic H-minority heating (although the absorption efficiency of 2^{nd} harmonic heating is uncertain [17]). Experiments were also conducted at 7.8 T using D(^{3}He) heating, which has reduced single-pass absorption, but neither I-mode nor H-mode were achieved with available power.

A typical C-Mod equilibrium shape for I-mode studies is shown in Fig. 1. The I-mode experiments mostly use an upper-single null divertor topology with "unfavorable" ion ∇B drift, i.e. with $B \times \nabla B$ pointed away from the primary X-point, which is known to increase significantly the auxiliary heating threshold to access H-mode as well as the threshold edge temperature [10, 11, 18]. Upper-null shapes can exploit strong divertor pumping for density control using the axisymmetric cryopump located there [19]. In addition, neon impurity seeding was often used in conjunction with pumping since this was found operationally to reduce high-Z impurity injections and generally improve plasma performance at high ICRF power. At the cryopump major radius the upper divertor has toroidal gaps (50% toroidal coverage) for particle entry to the pump volume (Fig. 1). However for $P_{ICRF} > 3$ MW we restrict the outer strikepoint to the inboard side of the entry gaps due to the reduced power handling of the entry gap tiles.

To date a small fraction (two cases, <5% of discharges) of the I-mode results have been obtained in lower single-null. In the first case the magnetic field direction was reversed from its usual direction so that lower-null has unfavorable ion ∇B direction. In the second case (a single discharge), I-mode was obtained with standard B direction and $B \times \nabla B$ pointed towards the primary X-point. The I-mode was the unintentional result of using an atypical geometry for C-Mod (green dashed line, Fig. 1) with low upper triangulatiry, high lower triangularity and small X-point clearance to the inner divertor during an experiment studying ELMy H-modes [20]. This shape is normally exploited on C-Mod for type I ELMy H-mode access and does not normally favor I-mode. It is not known what conditions favor I-mode in this particular geometry, but strikepoint location may play a role.

As a result of the C-Mod experimental campaign we have identified and examined ~100 I-mode timeslisces. A wide variety of heating power, plasma parameters and topologies has been explored: total heating power $P_{ICRF}+P_{ohmic} \equiv P_{tot} \sim 1.3$ -5.7 MW, $B_T \sim 3$-6 T, plasma current $I_p \sim 0.7$-1.3 MA, $q_{95} \sim 2.5 - 5$, plasma elongation $\kappa \sim 1.5 - 1.78$, primary divertor triangularity $\delta \sim 0.3 - 0.85$, and average $\delta \sim 0.35$ -0.6. Although experiments were carried out through a campaign where boronization films were applied for plasma performance [21], none of the I-mode experimental days used boronization immediately preceding the experiment. Wall conditions were therefore variable and, in contrast to EDA H-modes [22], apparently not critical.

Several key C-Mod diagnostic [23] locations are shown in Fig. 1. Thomson scattering (TS) and electron cyclotron emission (ECE) are used to provide electron density and temperature profiles in the core and pedestal region. Magnetic fluctuations are measured with an array of edge B-dot probes. Line-averaged density fluctuation spectra are measured with phase contrast imaging (PCI [24]). Edge density fluctuations are measured with a multi-frequency, outer midplane reflectometer system [25] and gas-puff imaging (GPI [26]). Edge and pedestal rotation and impurity analysis from B^{5+} charge-exchange recombination spectroscopy (CXRS) is presently limited to only a few cases at $q_{95} \sim 4.8$, $I_p = 0.8$ MA [15, 27].

3. Experimental Results

3.1. Identification of I-mode

In defining a confinement regime it is necessary to establish identifying features that make it distinct from standard L-mode confinement. For example, as auxiliary heating is increased an H-mode transition is experimentally identified by a sudden reduction in edge D-α recycling light, a positive break in slope of plasma density and stored energy, and the formation of an edge pressure pedestal. Previous studies [9, 15] showed that the I-mode was obtained in heating power ramps prior to H-mode, but featured neither a sudden D-α reduction nor a noticeable increase in density, making identification of the transition to from L-mode to I-mode problematic. To avoid circular logic it is unacceptable to identify a transition in confinement regime solely by its confinement quality factor (H).

Exploration of I-mode over a wider parameter space on C-Mod has shown that distinct transitions from L-mode to I-mode indeed exist and can be clearly identified in most cases. In particular L-I transitions become very distinct on C-Mod in discharges with low $q_{95} < 3.5$ and high heating power ($P_{ICRF} > 3$ MW), an example of which is shown in Fig. 2, in a discharge that features small increasing steps in P_{ICRF}. Fig. 2 also features a transition to ELM-free H-mode for comparison.

The L-I transition is most clearly identified by the rapid increase in pedestal temperature ($T_{e,95}$) from L-mode values, simultaneous with the power pulse from a sawtooth crash (Fig. 2 d-e). In contrast to the edge T response to the sawtooth heat pulses in the preceding L-mode, $T_{e,95}$ does not decay at the L-I transition but is instead maintained, and even increases further, following the barrier formation. Sawtooth crashes are always found to be the trigger for transitions to I-mode (and to H-mode) for the cases studied here. Where B^{5+} ion temperature T_i edge measurements are available from CXRS, they have also been found to increase and are equal to T_e within the uncertainties [27].

Through stiff core T profiles [5] the core temperature and stored energy increase as a result of the higher edge T_e. A confinement quality factor commensurate with H-mode [28], $H_{98,y2} \sim 1$ is obtained and maintained for more than 10 energy confinement times. However there is no noticeable change in the core density. The external fuelling rate (Fig. 2c, set by a feedback loop for density control with cryopumping) decreases gradually throughout the shot with its average value ~30% lower in I-mode than L-mode, yet active density control is maintained. Noticeable, but often weak, breaks-in-slope in D-α and P_{rad} also occur at the transition. The trend of the break-in-slope in P_{rad} is not consistent in all I-mode transitions, i.e. P_{rad} can sometimes increase or decrease at the L-I transition. The radiated power fraction (P_{rad}/P_{tot}) in I-mode tends to be relatively small and constant, varying between $P_{rad}/P_{tot} \sim 0.25$ - 0.4.

The transition to a transient ELM-free H-mode (at t=1.45 s in Fig. 2) contrasts sharply with the L-I transition. At the H-mode transition the density and P_{rad} rise rapidly and uncontrollably. Although RF heating power is constant, the subsequent decrease of conducted power to the pedestal/edge region due to core radiation from high-Z impurities, together with the increase in n_e, rapidly degrades the edge pedestal temperature and $H_{98,y2}$ decreases to ~0.5. These issues of transient ELM-free H-mode performance at low q_{95} and impurity accumulation with an uncoated high-Z wall have been previously documented on C-Mod [5, 21].

The evolution of the edge pedestal profiles is shown in Fig. 2g-h and Fig. 3. A large T_e pedestal gradient is established at the I-mode transition, and the T_e profile is comparable to that found in the H-mode. In contrast with H-mode, there is no significant change in the I-mode edge density or n_e gradient compared to L-mode. Only when a subsequent transition into the H-mode occurs is a clear density pedestal formed. It is this formation of an edge thermal transport barrier in the absence of an edge particle transport barrier which is the key feature of I-mode.

There are also marked changes in edge fluctuations at the transitions as shown in Fig. 2i-j. At the transition to I-mode there is a general decrease in low-frequency (~25-150 kHz)

broadband density/magnetic fluctuations (Fig. 2i), while simultaneously a weakly coherent density/magnetic fluctuation appears at higher frequencies (Fig. 2j). This is reminiscent of the quasi-coherent mode of EDA H-mode [22] but appears at higher frequency and is significantly broader in frequency. At the transition to H-mode the weakly coherent mode (WCM) promptly disappears, along with a general sharp reduction in broadband fluctuations. Based on multi-frequency reflectometry the WCM shown in Fig. 2 only exists between the 88 GHz and 110 GHz cutoff, which squarely places it in the I-mode T_e pedestal region between $0.9 < r/a < 1.0$ (Fig. 3b). The fluctuation characteristics, including their behavior at transitions, are examined in more detail in Sec. 3.5.

In summary there are several means to identify I-mode. The C-Mod experience has been that the *sudden* I-mode transition based on increased $T_{e,ped}$ is only observed at low q_{95} (<4) and high plasma current (> 1 MA), while at higher q_{95} the transition from L-mode tends to be more gradual [10, 15]. On the other hand the signature I-mode fluctuations described above are universally observed in both gradual and sudden I-mode transitions. Therefore the criteria for the identification of an I-mode are that it:

1) Must show the formation of an edge T_e pedestal, either abruptly or gradually, without a significant change in the edge density profile as compared to L-mode,
2) Must show the appearance of a high frequency (> 100 kHz) weakly coherent magnetic/density mode (WCM) with an accompanying reduction in broadband fluctuations below the WCM frequency,
3) Must *not* show the signatures of an H-mode transition, namely an abrupt (< 1 ms) and sharp decrease in D-α along with a positive break-in-slope of the core density,

In addition to these three criteria, it is often observed that I-mode transitions show a break-in-slope of radiated power, stored energy and/or D-α that can also aid in identification of transitions (although this is not used as a primary criterion due to the inconsistency of these breaks).

These criteria have been used to identify ~100 timeslices on C-Mod in the I-mode confinement regime. Furthermore we have identified ~20 clear L-I transition cases, i.e. where the I-mode exhibited the abrupt formation of the T pedestal as shown in the example of Fig. 2. Time intervals just before ($< \tau_e$) the formation of an I-mode were selected for threshold analysis. Similarly, ~40 I-mode intervals just prior to H-mode (particle barrier) transitions were selected for I-H threshold analysis.

3.2. Access to I-mode and H-mode

The operational space of the discharges dedicated to I-mode studies is shown in Fig. 4. As expected, the density of I-mode is essentially identical to L-mode and ~1.5-2x lower than H-mode. The I-mode density tends to organize to and increase with plasma current, as does L-mode. It is also apparent that I-mode exists over a finite range of density at a given plasma current. As density is lowered (using pumping) below some threshold value, at fixed I_p and P_{ICRF}, the L-mode core radiated power fraction suddenly increases to near unity. This high core radiated fraction from high-Z impurities decreases the loss power to the edge and likely impedes the formation of the I-mode transport barrier (H-mode transitions are also absent at these lower densities). Conversely, as density is increased the subsequent increase in edge neutral pressure is problematic for ICRF antenna operations and heating often becomes too erratic to establish I-mode. In addition, at higher density, even if an I-mode transition occurs it can be as short-lived as a single sawtooth period (~10-20 ms) before an H-mode transition occurs. It remains unclear if the I-mode density is constrained primarily by operational limits with the heating technique or by underlying transition physics.

Fig. 5 shows that in general the required heating power ($P_{loss} \equiv P_{tot} - dW/dt$) to obtain I-mode overlaps well with the range of heating power to obtain H-mode (except as noted, all discharges have unfavorable ∇B). This observation is supported by examining the power requirements to trigger L-I and I-H transitions (Fig. 6a) established through small-range B/I_p scans at fixed ICRF heating frequencies. It has been found that the threshold P_{loss} for

I and H mode transitions organizes well to q_{95} (although the 50 MHz, low B results of Fig. 5 and Fig. 6a show that there is a B dependence as well). The ratio of measured L-I and I-H threshold power to the widely used H-mode threshold power scaling $P_{LH,scaling}$ [29] is shown in Fig. 6b. The ratio $P_{loss}/P_{LH,scaling}$ is greater than unity as expected for unfavorable ∇B drift direction. However the approximately linear inverse q_{95} (I_p) dependence we find for the power threshold power does not appear in the standard H-mode threshold scaling prediction [29] and therefore appears to be a feature unique to unfavorable ∇B drift topology. This leads to a strong dependence on q_{95} for the "normalized" power to access I- or H-mode, with $P_{loss}/P_{LH,scaling} \sim 1.5\text{-}2.5$ at $q_{95} \sim 3$ and $P_{loss}/P_{LH,scaling} \sim 1.25$ at $q_{95} \sim 4.5\text{-}5$. A noteworthy exception to these trends is the one lower-null I-mode case with $B \times \nabla B$ towards the X-point (Fig. 6) which has a substantially lower I- and H-mode power threshold and closely follows the scaling prediction, i.e. $P_{loss}/P_{LH,scaling} \sim 1$.

Operational experience on C-mod has suggested that higher triangularity also plays a role in easing access to I-mode. This trend is difficult to quantify precisely due to the requirement for continuous upper divertor sweeping (and hence sweeping in triangularity) in order to avoid heating limits in the upper divertor (Fig. 1). Nevertheless is a regular trend for the L-I transition to occur in otherwise stationary discharges as upper triangularity was increased. In addition, the single I-mode transition with favorable ∇B topology in lower-null was found as lower triangularity was increased (Fig. 1) from one discharge to the next. Sec. 3.3 will show that energy confinement of I-mode also depends on triangularity.

3.3. Global characterization of I-mode energy, particle & momentum transport

The I-mode has energy confinement properties that set it apart from L- and H-mode. Fig. 7 shows the I-mode plasma stored energy (W_{th}) versus the product of total heating power P_{tot} and plasma current I_p. Since energy confinement time $\tau_e \equiv W_{th}/P_{tot}$ is known to be $\propto I_p$, (e.g. [28]) the observation that I-mode W_{th} increases nearly linearly ($\alpha=1$ in Fig. 7) with

$P_{tot} \cdot I_p$ indicates that the I-mode features a weaker degradation of energy confinement ($\tau_e \propto P^{\alpha-1}$) with heating power than seen in L-mode (α=0.5) or H-mode (α~0.3). At this point it is not possible to provide a reliable regression analysis for the I-mode W_{th} due to the strong correlations between I_p, n_e and P_{tot}. Nevertheless the trend of weak power degradation in I-mode is confirmed by examining a subset of I-mode discharges (green squares of Fig. 7) featuring a significant scan in heating power (P_{tot} = 3.3 MW to 5.1 MW) at fixed I_p~1.2 MA and density (n_{20}~1.9± 0.1) In these cases, W_{th} appears to increase linearly with P_{tot} with no sign of rollover. A power law fit of these fixed I_p ~1.2 MA cases yields α~0.7, consistent with the overall trend of W_{th} vs. $I_p \cdot P_{tot}$ in I-mode at B~5.5 T. The trend in W_{th} is less clear at lower B ~ 3-3.4 T, although this is likely affected by the uncertain absorption of the additional 2nd harmonic H-minority heating needed to access $P_{tot} > 3$ MW. The favorable trend of $W_{th} \sim P_{tot} \cdot I_p$, combined with the high heating power typical of low q_{95} I-modes, has allowed for stationary I-mode discharges with stationary volume-average pressure ~1.5 atm, which closely approaches the C-Mod absolute performance (1.8 atm) record set in H-mode using between-shot boronizations [21].

I-mode has an energy confinement roughly consistent with predictions of standard H-mode scaling over a wide range of parameter space. The confinement quality factor, $H_{98,y2}$ of I-mode lies in a narrow range near one as shown in Fig. 8 versus total heating power and q_{95}. Note, however, that I-modes are *not* identified by $H_{98,y2}$. The general trend of increasing H_{98} with heating power is consistent with the weaker than expected power degradation shown in Fig. 7. The notable exceptions to this trend are I-modes with atypical shape for I-mode, i.e. favorable ∇B drift or lower-single null shapes with reversed B, both which obtain high H_{98} at P_{tot} ~ 2 MW. This suggests that further increases in performance may be achievable. Also, the lower field I-mode cases have consistently lower H_{98} than at nominal field B~5.4 T. Fig. 8b shows that $H_{98,y2}$ ~0.9 -1.1 can be obtained over a wide range of q_{95} with a greater tendency for high H_{98}~1 values at lower $q_{95} < 3.5$. This contrasts with EDA H-mode which is strongly favored by $q_{95} > 3.5$ [30, 31]. The favorable ∇B drift I-mode again stands apart from this trend with H_{98}~1.1-1.2 at intermediate q_{95}~3.8.

The H_{98} confinement quality is plotted versus upper triangularity in Fig. 9 for a subset of the I-mode cases with the following characteristics: upper null (Fig. 1), 5.3 T < B < 5.9 T, q_{95} < 3.5. With fixed lower triangularity, the H_{98} factor clearly increases with upper triangularity (τ_{98} has no dependence on triangularity). Increasing lower triangularity at the smallest upper triangularity also appears to increase H_{98} (blue point in Fig. 9), but this has not been confirmed with systematic scans. These results again suggest means for further optimization of the I-mode shaping.

Fig. 10 compares global impurity confinement time to H_{98} energy confinement quality for L-mode, I-mode and stationary EDA H-modes [32, 33]. Impurity confinement time (τ_I) is obtained following laser ablation injection of calcium fluoride (CaF_2) films and the measurement of the central plasma Ca emission decay time with x-ray spectroscopy [34]. Ca injections into ELM-free H-modes have confinement times significantly longer than the duration of the H-mode (i.e. > 0.2-0.5 s) and so cannot be analyzed for τ_I. I-mode has energy confinement consistent with H-mode, but with the weak impurity particle confinement of L-mode (τ_I ~ 20-40 ms ~ τ_e). I-mode particle confinement time is considerably less than that found in stationary EDA H-modes. These observations are consistent with the fact that indicators of global particle confinement time are essentially unchanged between L- and I-mode: e.g. neither fuelling rate requirements (Fig. 2) nor density profiles (Fig. 3) are significantly modified.

Consistent with the Ca transport, global impurity levels are found to change by small factors (< factor of two) when transitioning from L-mode to I-mode. At q_{95}~4.8 the I-mode boron concentration is radially uniform and f_B~0.5% [27], approximately double that found in the preceding L-mode (boron is usually the dominant low-Z impurity in C-Mod). However visible bremsstrahlung and resistivity analyses indicate Z_{eff} ~ 1.4-1.6 in this case. Since f_B=0.5% leads to only ΔZ_{eff} = 0.1, it is inferred that high-Z molybdenum, with f_{Mo} ~ 0.03%, predominately sets the Z_{eff} increment. I-modes discharges at higher absolute confinement (q_{95}~3) have increased Z_{eff}~2-2.3. This is qualitatively consistent with a general increase of radiated power fraction from P_{rad}/P_{tot} ~0.25 at q_{95}> 4.5 to P_{rad}/P_{tot}

~0.4 at q_{95}~3. In cases where neon seeding is used to improved ICRF performance Z_{eff} is found to be higher (ΔZ_{eff} ~0.6) than matched shots without seeding. However, absolute plasma performance (e.g. stored energy, neutron rate) is unaffected or improved by seeding.

I-mode plasmas also feature core intrinsic rotation behavior similar to that found in EDA H-mode. Fig. 11 shows the increment in core toroidal rotation velocity as a function of the increment of stored energy normalized to plasma current with the application of ICRF heating (which does not directly apply torque to the plasma). The I-mode results follow the same approximately linear relationship with $\Delta W_{th}/I_p$ as found for a database of stationary EDA H-modes [35]. Since the I-mode increase in stored energy is solely from a T increase, rather than from density, this result suggests that temperature, rather than density or pressure, may play the more important role in setting intrinsic rotation.

3.4. I-mode Edge Pedestal: Profile characteristics

I-mode pedestal density and temperature profiles, including both core and edge Thomson scattering and ECE, have been fitted (e.g. Fig. 3) to the modified hyperbolic function conventionally used for H-mode pedestal analysis [36]. These fits include timeslices from the I-mode campaign (Fig. 4), as well as example stationary EDA H-modes from earlier pedestal scaling studies [37] and recent ELMy H-modes, the latter two with favorable ∇B drift topology.

The I-mode discharges are on a lower collisionality T vs. ν^* track than H-mode. Fig. 12 shows the pedestal electron temperature versus pedestal neoclassical collisionality, ν^*_{95} (see for example [38]). I-mode significantly expands the C-Mod operational space of stationary ELM-free regimes: from the collisional ($\nu^*_{95} > 1$) L-mode/EDA regimes with $T_{ped} < 0.4$ keV to the collisionless ($\nu^*_{95} \sim 0.1$) I-mode with T_{ped} approaching 1 keV.

For completeness, it should be noted that small, infrequent ELMs have occasionally been seen in I-mode. These ELMs are almost always triggered by a sawtooth pulse (similar to I-H transition triggers). The ELMS are quite small in size with $\Delta T/T_{ped}$ ~5-10% i.e. smaller than edge perturbations caused by the sawteeth. Stored energy loss from the ELM is small enough in magnitude so as to make its measurement difficult in the presence of sawtooth crashes. For the infrequent case of an ELM not triggered by a sawtooth crash we roughly estimate from magnetics and kinetic profiles: $\Delta W_{ELM}/W_{th}$~0.5-1.5% and $\Delta W_{ELM}/W_{ped}$~ 2-5%. Given the pedestal collisionality ν^*_{ped} ~0.2 in this case, we make a preliminary assessment that these belong in a "small" ELM category as compared to normalized ELM energy loss from other devices [38]. Whatever their characteristics, these ELMS play a minimal role in regulating core particle or impurity content during I-mode. To date we have not identified a particular operational condition(s) that causes these infrequent ELM; more often the I-mode phases are completely free of ELMs (e.g. Fig. 2).

The T_e gradient scale-length (L_T) and the n_e gradient scale-length (L_n), both evaluated at the symmetry point of the T pedestal (i.e. the location of minimum L_T), are shown in Fig. 13. Like H-mode, I-mode tends to have substantially smaller L_T than L-mode, consistent with the formation of an edge thermal transport barrier. However L_n of I-mode is ~10 times larger than in stationary EDA H-modes, consistent with the lack of an edge particle transport barrier.

The stability parameter ($\eta_e \equiv L_n/L_T$) in the pedestal is shown in Fig. 14 as function of q_{95}. It is found that the stationary H-modes exist in a narrow stability space of η_e ~ 1-2 for EDA (as previously seen on C-Mod [39]) and η_e ~ 2-4 for ELMy H-modes with no strong dependence on q_{95}. This clustering of η_e has also been reported on ASDEX-Upgrade [40]. In contrast I-mode discharges have a much higher of η_e, up to ~60, and show a consistent trend that the minimum observed η_e decreases with increasing q_{95} regardless of B field or ∇B drift direction. This is another clear delineation of I-mode from H-mode, particularly at lower $q_{95} < 3.5$, and may have implications for the dominant turbulence mechanisms in I-mode.

3.5. I-mode Edge Pedestal: Fluctuations

An important identifying aspect of I-mode involves edge fluctuations (Sec 3.1), and in particular a weakly coherent mode (WCM) which is found to be concurrent with I-mode. Table 1 contains the results of spectral analysis of magnetic and density fluctuations for sample discharges in two ranges of q_{95}/I_p.

The WCM is an electromagnetic mode which exists in the outboard pedestal region of I-mode plasmas. Based on the cutoff density, multi-frequency reflectometry locates the WCM between r/a ~ 0.9 -1.0 (e.g. Fig. 3). Gas-puff imaging (GPI) at q_{95} ~ 3 has also shown that the mode persists at least in to r/a~0.9 on the outboard side (the inner limit of the GPI measurement), and is slightly peak at r/a ~ 0.95, but does not exist outside the separatrix. Like the quasi-coherent (QC) mode found in EDA H-mode [30], the mode propagates poloidally in the electron diamagnetic direction in the lab frame. The WCM propagates toroidally in the counter-current direction, consistent with a field-aligned ($\mathbf{k}\cdot\mathbf{B}$=0) mode. The relative frequency broadening of the time-averaged spectrum is much larger for the WCM ($\Delta f/f_{max}$~0.5) than for the QC mode ($\Delta f/f_{max} < 0.2$) [30]. Analysis of the WCM indicates that the frequency at which the peak spectral magnitude occurs swings rapidly throughout the frequency band of the mode. This may indicate a set of coupled modes existing over a wide frequency range.

Table 1 shows how the WCM characteristics change as q_{95} is decreased from q_{95}~4.8 to q_{95}~3: peak frequency and width are increased, toroidal mode number n doubles from 10 to ~20, and the poloidal phase velocity increases from ~3 km/s to ~8 km/s. GPI and PCI measurements indicate the poloidal wavenumber on the outboard midplane, k_{pol} ~ 150-200 m^{-1}, does not change appreciably with q_{95} which provides a rough estimate of m/n ~ 6 at q_{95}~4.8 decreasing to m/n~3 at q_{95}~3, self-consistent with an edge mode at r/a > 0.9. The wavenumber of the WCM is of similar magnitude to that found for the QC-mode in EDA H-mode (k_{pol} ~ 250-300 m^{-1} from PCI[30]). The WCM toroidal phase velocity >

+50 km/s is opposite in sign to, and substantially larger in absolute magnitude, than the pedestal's typical I-mode co-current plasma toroidal velocity ~ -10 km/s as measured with B^{5+} CXRS [27], indicating that the WCM also has a high frequency in the plasma frame. Simultaneous measurements of poloidal phase and fluid velocity are not yet available.

Fig. 15 highlights a discharge with several confinement mode transitions (at constant ICRF heating) and the corresponding behavior of the magnetic and density fluctuations. The heat pulse from a sawtooth crash triggers all transitions to I-mode or H-mode. In I-mode, the weakly coherent mode (WCM) at ~200 kHz is present on both magnetic and density fluctuations, and is accompanied by a reduction in broadband fluctuation amplitude at frequencies between ~50 kHz and the WCM frequency as compared to L-mode. The WCM is immediately terminated, along with fluctuations at other frequencies, by a transition to ELM-free H-mode. The broadband fluctuation amplitude increases at the back-transition to L-mode at 0.95 s. The WCM appears simultaneously with the formation of the I-mode T pedestal triggered by the sawtooth. In some instances there is a slight upsweep in WCM frequency after the L-I transition. This is in contrast with the QC-mode which sweeps down in frequency at its onset, presumably due to Doppler shifts as the plasma rotation evolves after the L-H transition [30].

The brief transition to H-mode at 0.83 s for ~15 ms (~1/3 τ_e) and transition back to I-mode is illustrative. With the decease of the WCM the density starts to increase with a slope similar to the longer ELM-free H-mode at 0.9 s. But the sudden recurrence of the WCM clamps any further increase in density in ~ms timescale. This strongly suggests that the WCM is directly responsible for regulation of the density (fuel or impurities) and the presence of the WCM is the cause of L-mode-like particle transport in the edge plasma. Yet, like the QC-mode, the WCM is compatible with an H-mode-like T pedestal and thermal transport barrier.

4. Discussion

The study of I-mode has two important motivations: 1) understanding transport and threshold physics and 2) developing optimized operational scenarios.

Pertaining to the first motivation, I-mode is a self-organized plasma state like H-mode, but one in which the energy and particle transport channels are clearly separated. This feature makes I-mode a valuable tool in exploring the underlying transport, as well as the physics associated with the transition to high confinement modes. The I-mode edge stability parameter (η_e) can span a very large range of values (Fig. 14) unlike H-mode. The fact that the minimum accessible η_e has a strong q_{95} dependence suggests that magnetic shear plays an important role in I-mode pedestal regulation. In addition, plasma shaping/triangularity is seen to have a significant effect on I-mode normalized performance, as it does in H-mode. In H-mode these dependencies are understood to be due to the important role of shaping on edge stability (e.g. peeling-ballooning for ELM onset [6], kinetic ballooning for transport [41]). Yet I-mode lacks a density pedestal, which obviously has important consequences for edge pressure profiles and the resulting self-consistent edge bootstrap currents important for stability. Along with the lack of ELMs, these observations suggest that I-mode is exploring a somewhat different (and interesting) part of the edge stability space than standard H-mode. Like the QCM of EDA H-mode, I-mode has a short wavelength, edge MHD mode (WCM) that appears to regulate particle transport. However the QCM favors high q_{95} and collisionality, while the WCM can manifest at low q_{95} and low collisionality. Taken together the observations above argue that I-mode has a different set of feedback mechanisms between the underlying turbulence, the profile/gradient plasma fields and accompanying MHD stability. The cross-correlation among the fluctuation fields is also likely to be different in I-mode in order to permit significant cross-field turbulent particle transport, yet highly suppressed energy transport, in a collisionless edge plasma.

Furthermore, the prevalence of I-mode with BxVB pointed away from the X-point would seem to provide clues as to the long-standing mystery of higher threshold powers with

that configuration. The I-mode simultaneously features a definite, but relatively weak, E_r well in the pedestal [15] and rotation profiles that evolve in a different way than H-modes [27]. Previous C-Mod studies of SOL flows and core rotation have shown that strong transport-driven flows in ohmic plasmas are in opposite directions in the favorable and unfavorable configurations, thus modifying the boundary conditions for rotations in the confined plasma [42, 43]. Yet the I-mode threshold in power is very similar to that found for H-mode, while no particle barrier is formed. It seems valuable to use both the similarities and differences of I-mode vs. H-mode to uncover the underlying mechanisms controlling transitions to high-energy confinement regimes.

Pertaining to the second motivation, I-mode exhibits operational scenario advantages that make it highly attractive. I-mode features a high temperature, low collisionality pedestal without ELMs, a condition which will be required in ITER and other future large scale fusion devices. I-mode simultaneously provides impurity and density control in an ICRF-heated high-Z wall tokamak without the requirement of immediately preceding boronizations. In addition, power handling in the divertor should be greatly aided by a broader L-mode SOL profile (Fig. 3). The I-mode stored thermal energy increases nearly linearly with heating power. I-mode certainly exhibits its best absolute and normalized performance at low q_{95} and high heating power, which makes its generally attractive for high fusion power density scenarios ($P_{heating}/S_{plasma} \sim 0.25$ MW/m^2 in ITER [2], P/S ~ 0.7-1 MW/m^2 in C-Mod and reactors [3]). A possible difficulty in exploiting I-mode in ITER is the high power generally required to trigger the L-I transition (Fig. 6). However it should be noted that in several individual cases, the threshold power is within <25% of the standard H-mode threshold scaling. It seems premature to assess if ITER can access I-mode at this time. But expanding access to I-mode at lower power densities, and in other magnetic topologies, would be valuable in determining its general applicability as an operational regime.

5. Conclusions

An improved energy confinement regime, I-mode has been studied in the Alcator C-Mod tokamak. I-mode features an edge energy transport barrier without a strong accompanying particle barrier. To date I-mode has primarily been accessed in C-mod with the following experimental conditions: upper-null topology with high upper triangularity and BxΔB pointed *away* from the primary X-point, on axis H(D)-minority ICRH plasma heating and divertor cryopumping for density control.

H-mode energy confinement is obtained without core impurity accumulation. As a result, I-mode has stationary and reduced impurity radiation as compared to H-modes previously obtained with a high-Z metal wall and ICRF heating. I-mode also features a stationary edge pedestal, which usually is completely free of ELMs. I-mode is a confinement regime that appears distinct from both L-mode and H-mode, both in its global performance and in its local pedestal and fluctuation characteristics.

Acknowledgments

This work was supported by U.S. DOE Cooperative Agreement DE-FC02-99ER54512.

List of Figures

Fig. 1 Example upper single-null equilibrium used for I-mode studies (red separatrix) with BxVB pointed away from the X-point (upper null discharge of Fig. 2). Also shown is the separatrix (green dashed line) for the I-mode case with BxVB pointed toward the X-point in lower single null. The upper divertor cryopump, pump entry gaps and key diagnostic locations are indicated.

Fig. 2 Example upper single-null B=5.6 T, q_{95}~3.2 I-mode discharge with divertor cryopumping (Fig. 1) with L-mode, I-mode and ELM-free H-mode phases indicated. (a) plasma current and ICRF heating power, (b) D-α recycling and core radiated power, (c) D_2 gas fuelling rate and line-averaged density $\bar{n}_e$, (d) $T_{e,95}$ pedestal electron temperature at r/a~0.95 from ECE, (e) $T_{e,0}$ central electron temperature, (f) stored thermal energy W_{th} and confinement quality $H_{98,y2}$ (g) pedestal T_e gradient evaluated from edge TS, (h) local density at pedestal (r/a~0.95) and separatrix (r/a~1.0) from TS, (i) poloidal magnetic field fluctuation amplitude averaged over the frequency range 100-150 kHz from $\tilde{B}_\theta$ coils (Fig. 1), (j) density fluctuation amplitude spectrum from outer midplane reflectometery at 88 GHz.

Fig. 3 Examples of radial profiles from the outer third of the plasma for L-mode, I-mode and ELM-free H-mode phases as indicated by vertical gray bars on Fig. 2. Profiles are fitted to a modified tanh function. Slices are shown in (a) electron temperature from Thomson scattering and ECE (b) electron density from Thomson scattering. The reflectometer 88 GHz (Fig. 2j) cutoff density is shown.

Fig. 4 Line averaged density versus plasma current over the experimental range of I-mode discharges studied, plus accompanying parameters for L-mode (preceding I-mode) and H-mode phases (ELM-free) in same discharges. I-modes at low B are separately plotted.

Fig. 5 Loss power, P_{loss} ($\equiv P_{ICRF}+P_{Ohmic}-dW_{th}/dt$), versus edge safety factor q_{95} over the experimental range of I-mode discharges studied, plus accompanying parameters for H-mode phases (ELM-free) in same discharges. I-modes at low B are separately plotted.

Fig. 6 Threshold P_{loss} values for transitions to I-mode and H-mode. The I-mode in lower null with BxΔB towards the X-point is circled in green (a) P_{loss} vs. q_{95} (b) Ratio of P_{loss} to ITER L-H power threshold [29] scaling ($P_{LH}[MW]=0.049 \cdot B[T]^{0.80} \cdot n[10^{20}\ m^{-3}]^{0.72} \cdot S[m^2]^{0.94}$).

Fig. 7 I-mode plasma stored thermal energy W_{th} versus the product of plasma current and total heating power. Dashed lines show W_{th} (or $\tau_e \sim W_{th}/P_{tot}$) dependence/degradation with heating power for cases: $\alpha = 0.31$ H-mode degradation [28], $\alpha = 0.5$ L-mode degradation, $\alpha = 1$ no power degradation. Green square symbols highlight a set of ~5.5 T I-mode discharges with a heating power scan at fixed plasma current of 1.2 MA.

Fig. 8 Confinement quality factor, $H_{98,y2}$ in I-mode versus (a) Total heating power P_{tot} (b) Edge safety factor q_{95}. Special cases are noted: BxΔB towards the X-point (green dashed circle) and lower single null with "reverse B", BxΔB away from the X-point (blue dashed circle).

Fig. 9 Confinement quality factor, $H_{98,y2}$ in I-mode versus upper triangularity for upper-null I-mode discharges with B~5.3 to 5.9 T and $q_{95} < 3.5$. Lower triangularity ranges are noted.

Fig. 10 Impurity particle confinement time (τ_I) as measured by impurity laser ablation injections) versus energy confinement quality $H_{98,y2}$ for L-mode, I-mode and EDA H-modes.

Fig. 11 Incremental increase (with ICRF heating) in plasma toroidal rotation $\Delta V_{toroidal}$ versus incremental increase in plasma thermal energy ΔW_{th} normalized to plasma current

I_p. I-mode results are compared to a database of EDA H-modes [35]: I-mode is consistent with H-modes indicating a scaling of $\Delta V \sim \Delta W_{th}/I_p$.

Fig. 12 Electron temperature as a function of neo-classical collisionality at r/a~0.95. The L-, I- and ELM-free H-mode results with BxVB away from the X-point are from the I-mode campaign. Note ELM-free points are non-stationary. From previous campaigns [37] stationary EDA, and recent ELMy H-modes, with standard BxVB towards the X-point are shown for comparison.

Fig. 13 Electron temperature gradient scale-length versus density gradient scale-length evaluated at the symmetry location of the T_e pedestal. The L-, I- and ELM-free H-mode results are from the I-mode campaign with BxVB away from the X-point while the EDA result [37] use standard BxVB towards the X-point.

Fig. 14 The ratio of density to temperature gradient scale-lengths η_e evaluated at the symmetry location of the T_e pedestal versus edge safety factor q_{95}. I-mode cases at low and standard B field are with BxVB away from the X-point except as noted. In I-mode η_e appears to have a minimum value which depends on q_{95} (dashed line). In comparison, η_e in EDA and ELMy H-modes with standard BxVB towards the X-point does not vary with q_{95}.

Fig. 15 Example of edge fluctuations in a discharge with a variety of confinement mode transitions. Stationary upper-null discharge parameters: BxVB away from the X-point, B_t=5.8 T, I_p=1.3 MA, q_{95}~3.2, constant ICRH power ~ 3.8 MW, elongation ~ 1.6, upper triangularity ~ 0.7. Fluctuation amplitude spectra of poloidal field (a) and density (b-c) from phase contrast imaging, PCI (b) and reflectometry (c) at 88 GHz (Fig. 3) which is only available after 0.8 s. PCI chord and $\tilde{B}_\theta$ coil locations are shown in Fig. 1. Other parameters: (d) pedestal T_e, (e) line-averaged density and core T_e and (f) midplane D-α recycling. Confinement modes are identified by colored regions: L-mode (white), I-mode (pink) and ELM-free H-mode (blue).

Table 1. Characteristics of the weakly coherent MHD edge feature in I-mode (BxVB away from the X-point, B~ 5.6 T). Sign conventions for k and phase velocity v_{ph}: positive toroidal = positive ϕ propagation (counter-current, Fig. 1), positive poloidal = electron diamagnetic drift direction (vertically upward at the outer midplane, Fig. 1).

Case	**High q_{95}**	**Low q_{95}**
q_{95}	4.5- 4.8	3 – 3.3
I_p (MA)	~ 0.8	~ 1.25
Magnetic fluctuations		
Peak frequency (kHz)	~ 120-150	~ 200-300
FWHM (kHz)	~ 60	~ 80-100
$k_{toroidal}$ (m^{-1}) / **n**	+12-15 / **8-10**	+30-37 / **20-25**
$V_{ph,toroidal}$ (km/s)	+ 75 - 110	+ 42 – 62
Density fluctuations – reflectometry / GPI / PCI		
Peak frequency (kHz)	~ 100	200-240
Peak FWHM (kHz)	~ 50	~ 80
$k_{poloidal}$ (m^{-1})	N/A / N/A / 210*	N/A / 150 / 210*
$V_{ph,poloidal}$ (km/s)	+ 3	+ 6 -10

* PCI $k_{pol} \sim k_R \sin(\pi/4)$ based on poloidal angle of flux surface at PCI chord (Fig. 1).
Shots: 1080415017, 1080416021, 1080416028, 1100204019

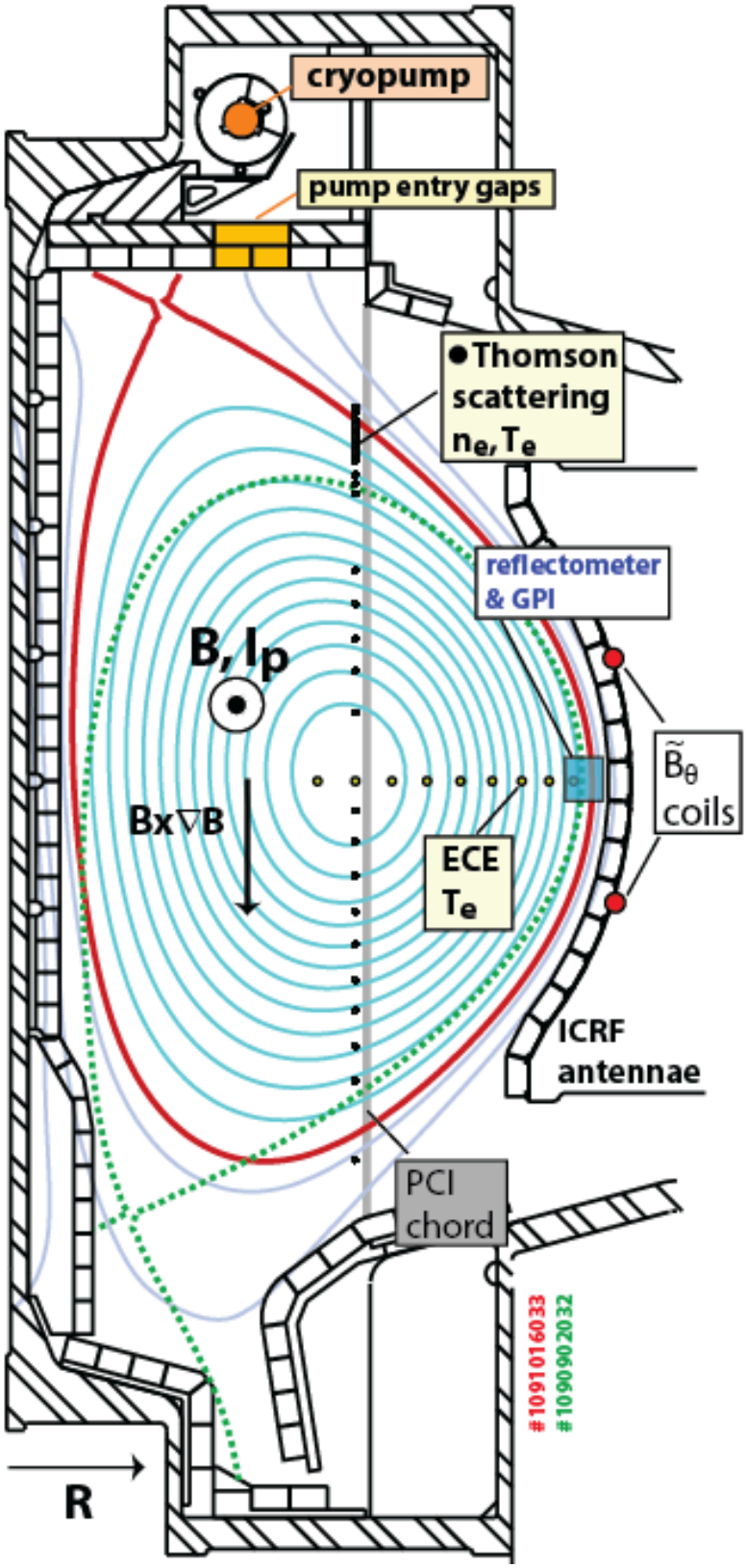
cryopump
pump entry gaps
Thomson scattering
n_e, T_e
reflectometer & GPI
B, I_p
Bx∇B
ECE
T_e
$\tilde{B}_\theta$ coils
ICRF antennae
PCI chord
#1091016033
#1090902032
R

Fig. 1

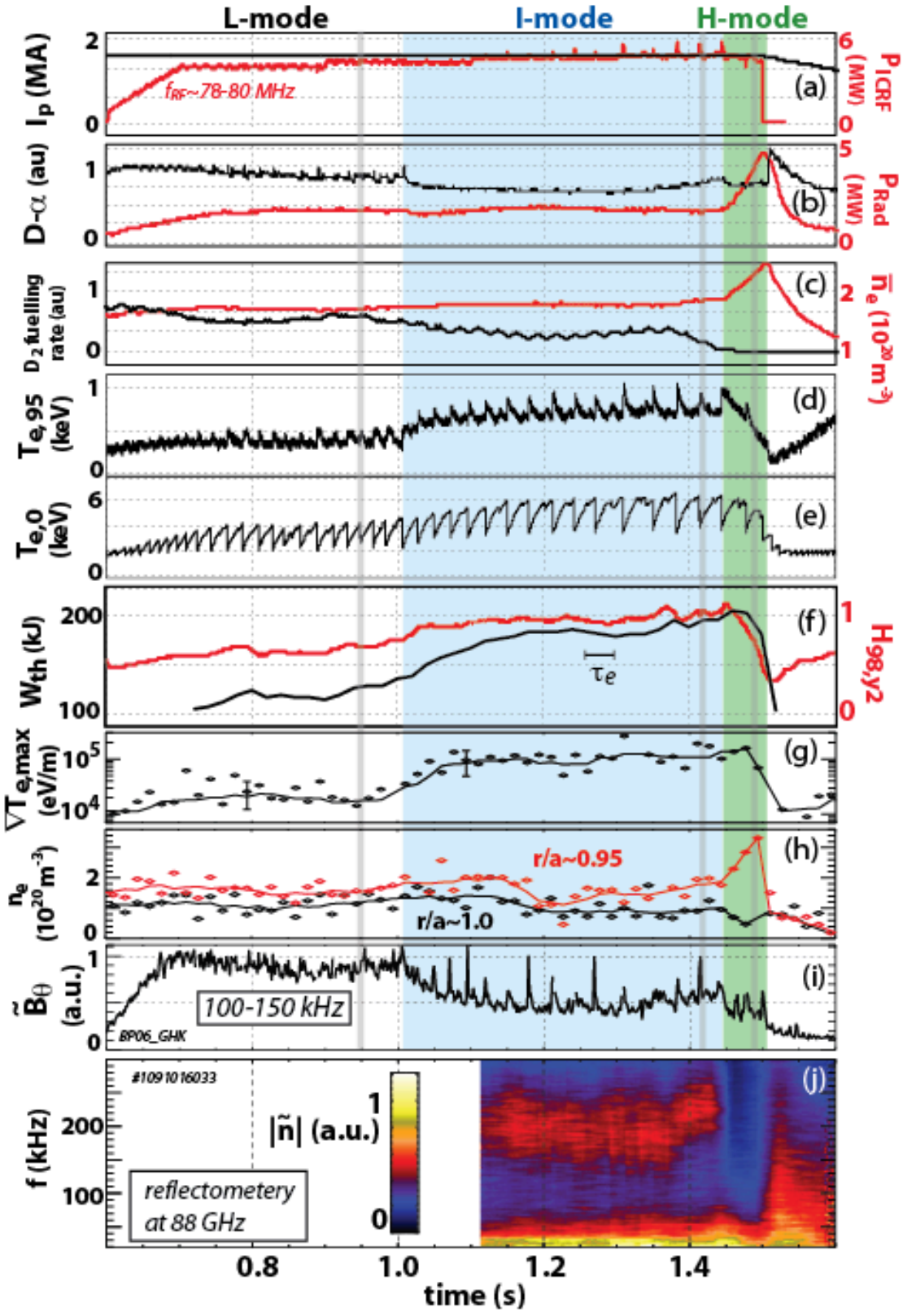
L-mode
I-mode
H-mode
I_p (MA)
f_{RF}~78-80 MHz
(a)
P_{ICRF} (MW)
D-α (au)
(b)
P_{Rad} (MW)
D_2 fuelling rate (au)
(c)
$\bar{n}_e$ (10^{20} m^{-3})
$T_{e,95}$ (keV)
(d)
$T_{e,0}$ (keV)
(e)
W_{th} (kJ)
τ_E
(f)
$H_{98,y2}$
$\nabla T_{e,max}$ (eV/m)
(g)
n_e (10^{20} m^{-3})
r/a~0.95
r/a~1.0
(h)
$\tilde{B}_\theta$ (a.u.)
100-150 kHz
BP06_GHK
(i)
#109016033
f (kHz)
$|\tilde{n}|$ (a.u.)
reflectometery at 88 GHz
(j)
time (s)

Fig. 2

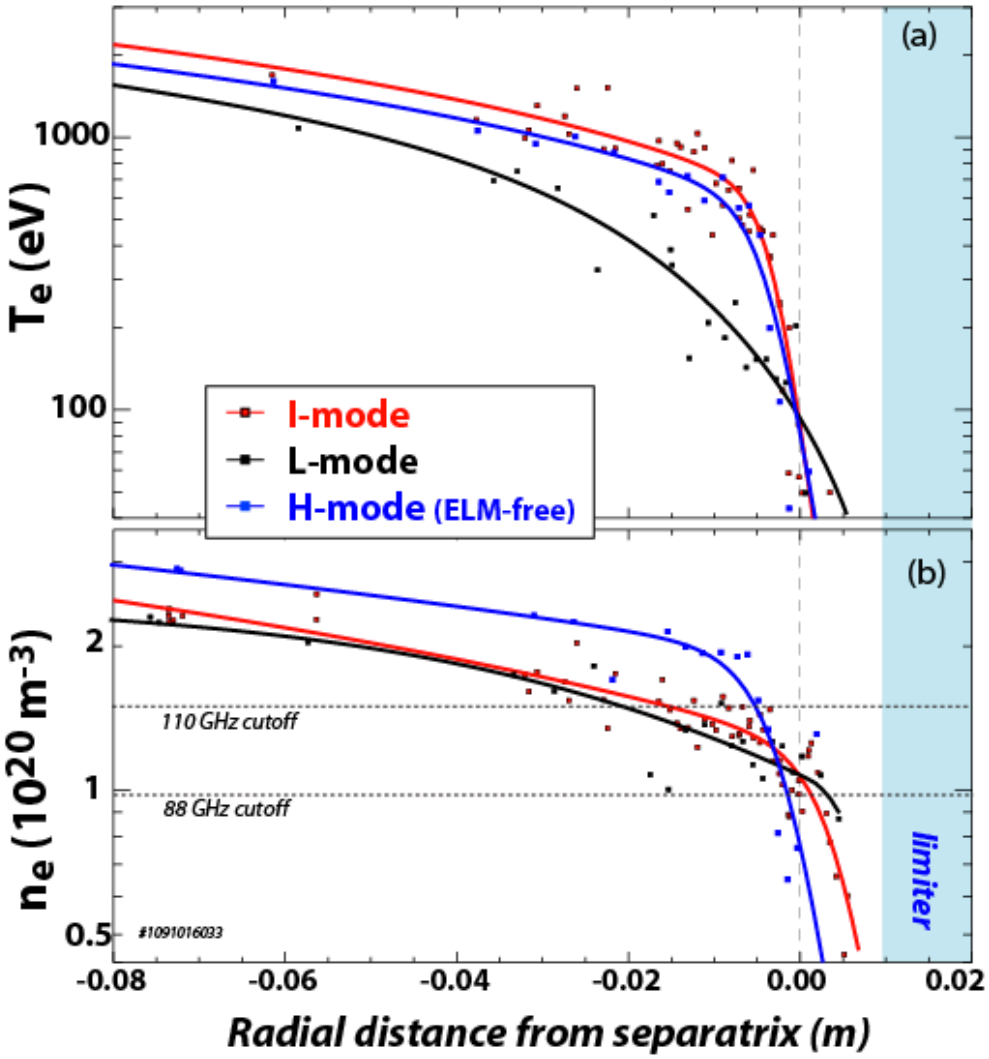
(a)
1000
100
T_e (eV)
I-mode
L-mode
H-mode (ELM-free)
(b)
2
1
0.5
n_e (10^{20} m^{-3})
110 GHz cutoff
88 GHz cutoff
#1091016033
limiter
-0.08
-0.06
-0.04
-0.02
0.00
0.02
Radial distance from separatrix (m)

Fig. 3

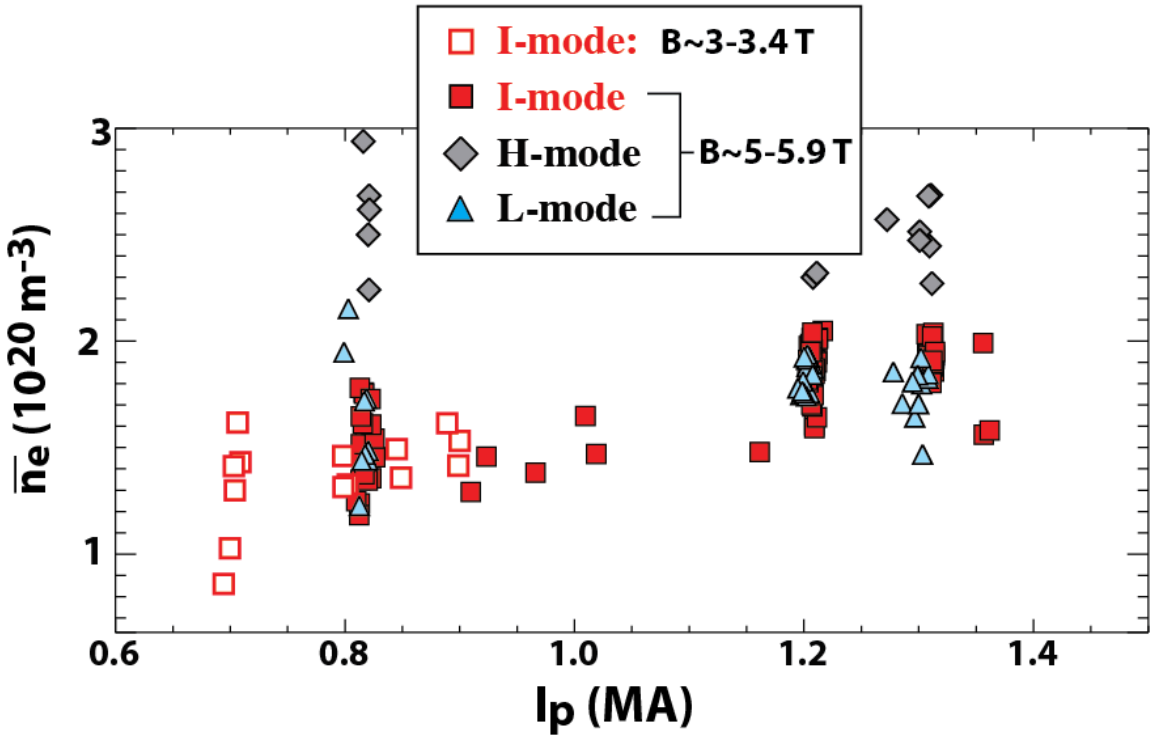
I-mode: B~3-3.4 T
I-mode
H-mode
L-mode
B~5-5.9 T
$\overline{ne}$ (10^{20} m^{-3})
3
2
1
0.6
0.8
1.0
1.2
1.4
Ip (MA)

Fig. 4

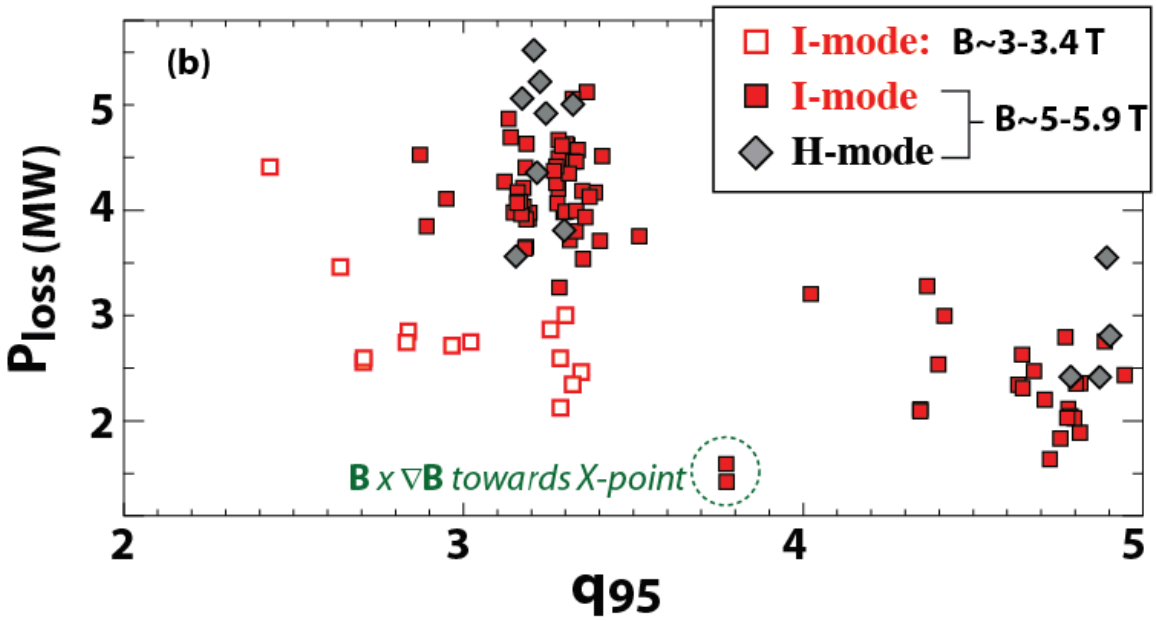
(b)
I-mode: B~3-3.4 T
I-mode
H-mode
B~5-5.9 T
B x ∇B towards X-point
P_loss (MW)
q95
2
3
4
5

Fig. 5

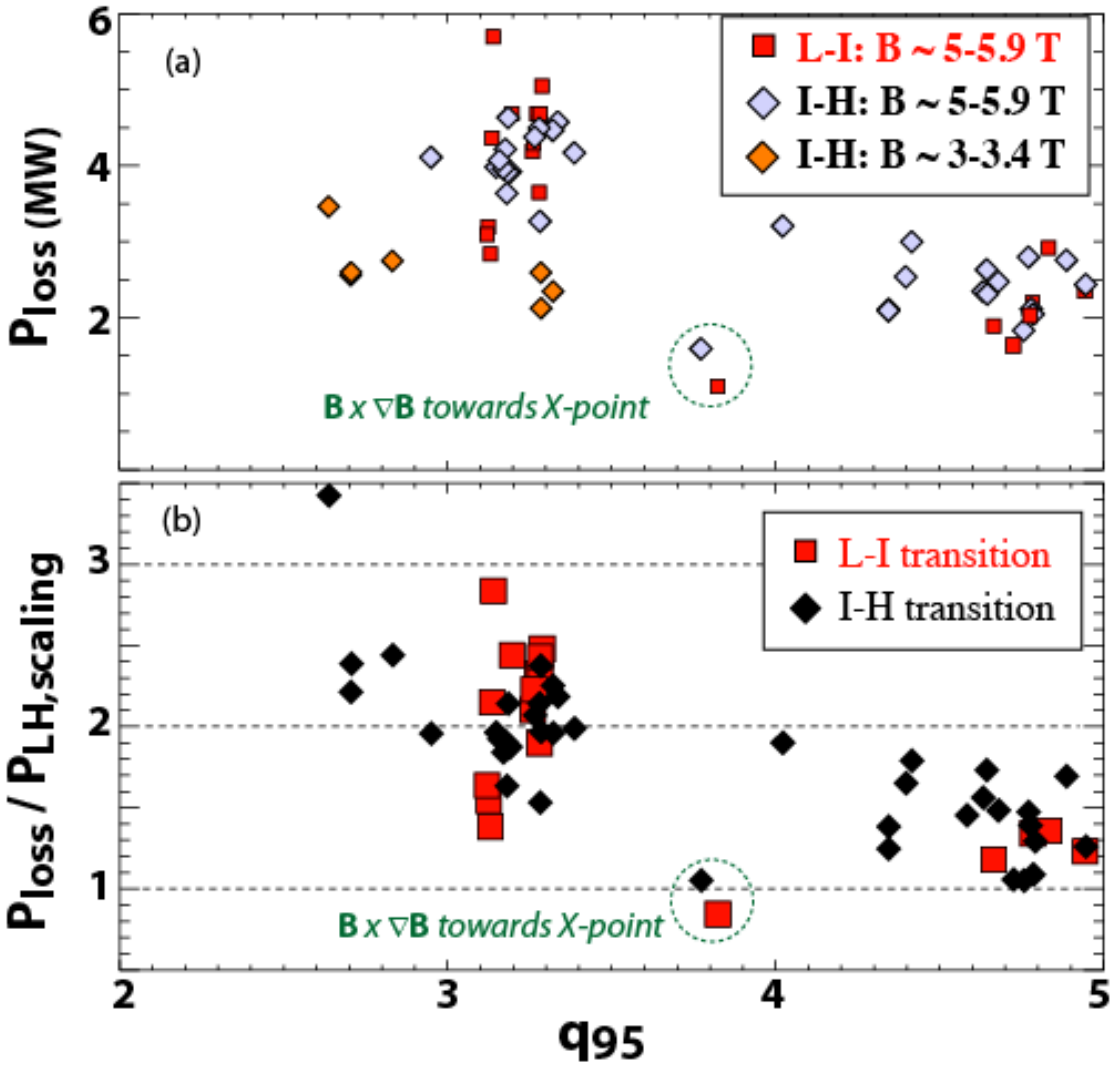
(a)
L-I: B ~ 5-5.9 T
I-H: B ~ 5-5.9 T
I-H: B ~ 3-3.4 T
B x ∇B towards X-point
P_loss (MW)
(b)
L-I transition
I-H transition
B x ∇B towards X-point
P_loss / P_LH,scaling
q95

Fig. 6

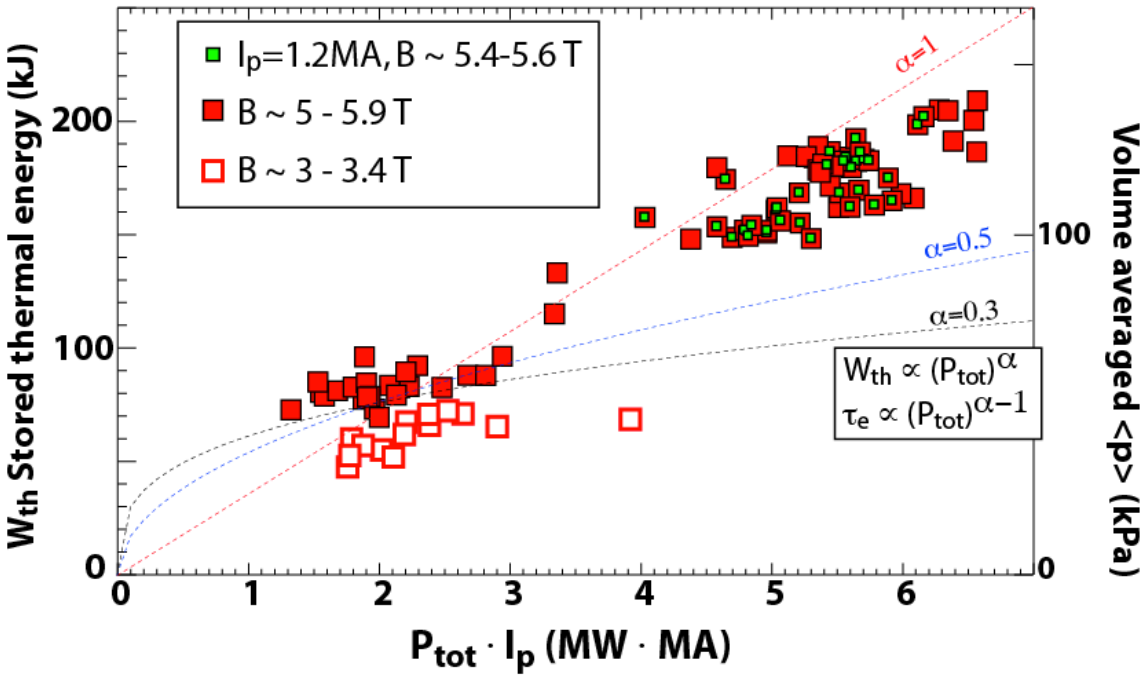
I_p=1.2MA, B ~ 5.4-5.6 T
B ~ 5 - 5.9 T
B ~ 3 - 3.4 T
α=1
α=0.5
α=0.3
$W_{th} \propto (P_{tot})^{\alpha}$
$\tau_e \propto (P_{tot})^{\alpha-1}$
W_{th} Stored thermal energy (kJ)
Volume averaged <p> (kPa)
$P_{tot} \cdot I_p$ (MW · MA)
0
100
200
0
1
2
3
4
5
6
0
100

Fig. 7

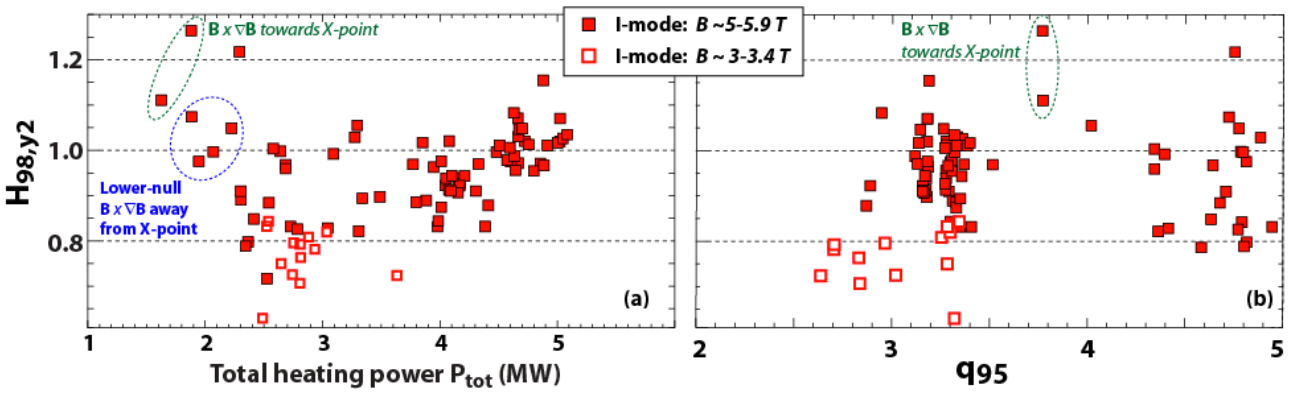
B x ∇B towards X-point
I-mode: B ~5-5.9 T
I-mode: B ~ 3-3.4 T
B x ∇B towards X-point
Lower-null B x ∇B away from X-point
H98,y2
1.2
1.0
0.8
(a)
(b)
1
2
3
4
5
Total heating power Ptot (MW)
q95

Fig. 8

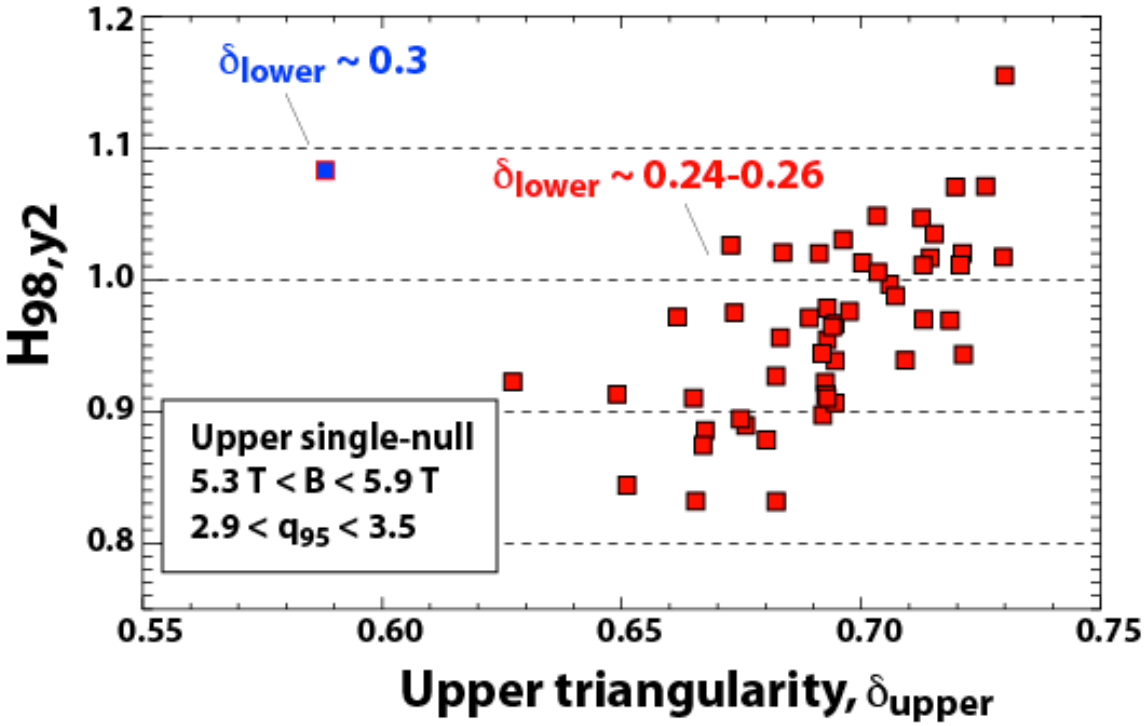
1.2
1.1
1.0
0.9
0.8
H98,y2
δlower ~ 0.3
δlower ~ 0.24-0.26
Upper single-null
5.3 T < B < 5.9 T
2.9 < q95 < 3.5
0.55
0.60
0.65
0.70
0.75
Upper triangularity, δupper

Fig. 9

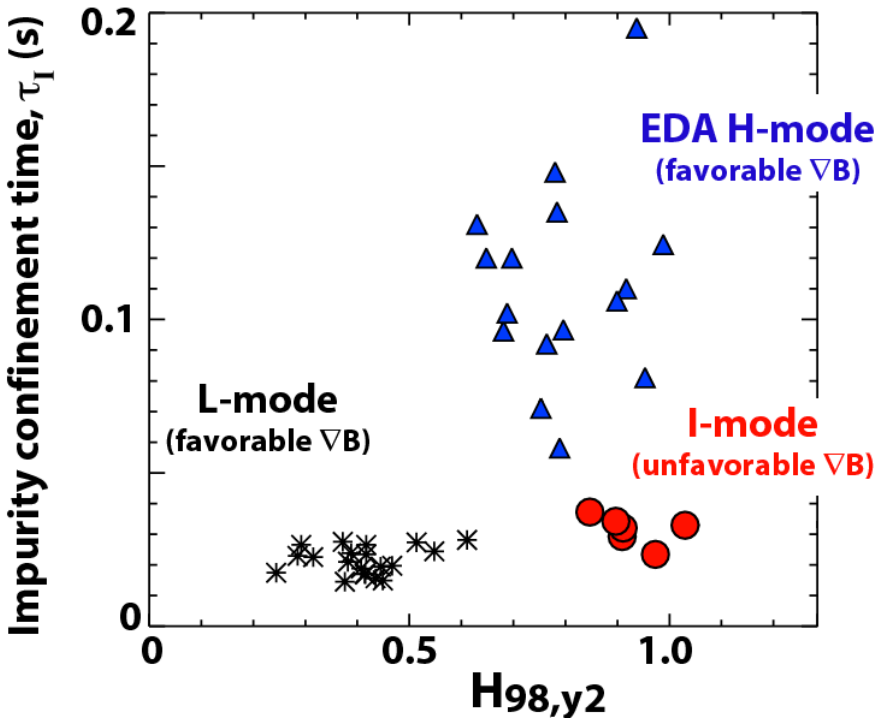
Impurity confinement time, τ_I (s)
0.2
0.1
0
0
0.5
1.0
$H_{98,y2}$
EDA H-mode
(favorable ∇B)
L-mode
(favorable ∇B)
I-mode
(unfavorable ∇B)

Fig. 10

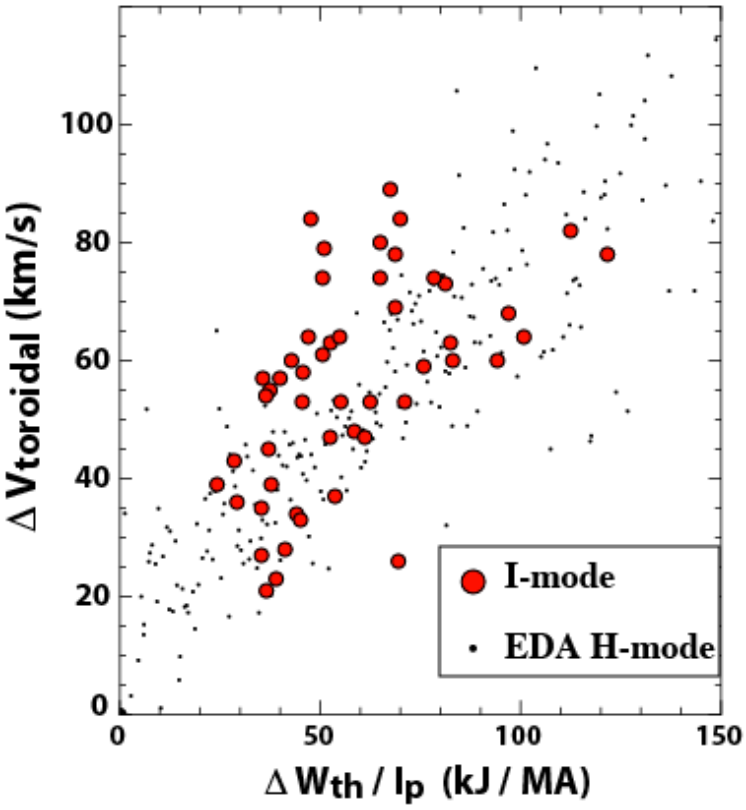
100
80
60
40
20
0
0
50
100
150
Δ Vtoroidal (km/s)
Δ Wth / Ip (kJ / MA)
I-mode
EDA H-mode

Fig. 11

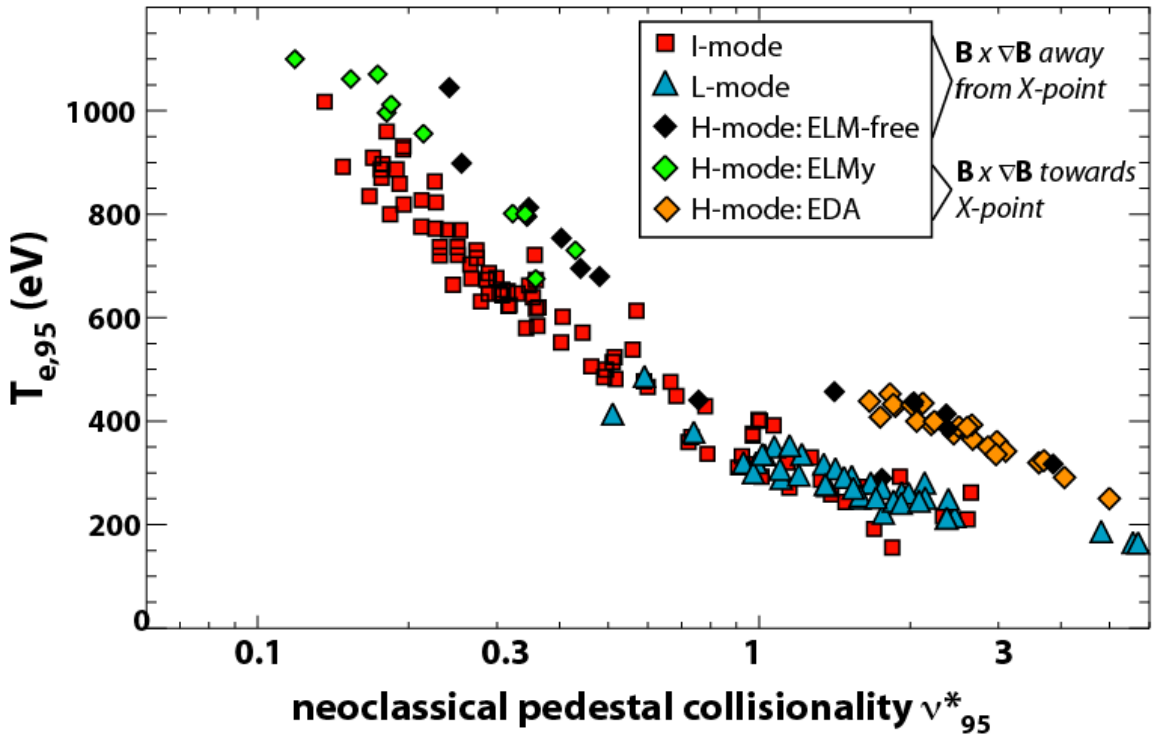
I-mode
L-mode
H-mode: ELM-free
H-mode: ELMy
H-mode: EDA
B x ∇B away from X-point
B x ∇B towards X-point
1000
800
600
400
200
0
0.1
0.3
1
3
T_e,95 (eV)
neoclassical pedestal collisionality ν*_95

Fig. 12

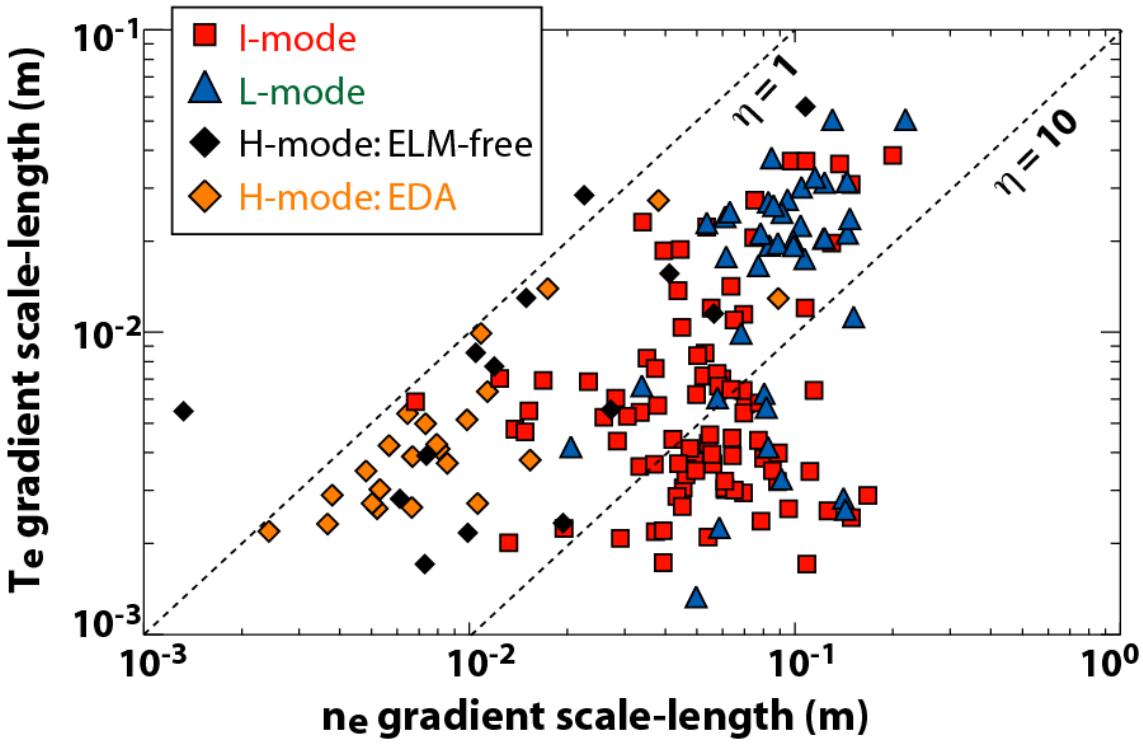
I-mode
L-mode
H-mode: ELM-free
H-mode: EDA
η = 1
η = 10
10^{-1}
10^{-2}
10^{-3}
10^{-3}
10^{-2}
10^{-1}
10^{0}
T_e gradient scale-length (m)
n_e gradient scale-length (m)

Fig. 13

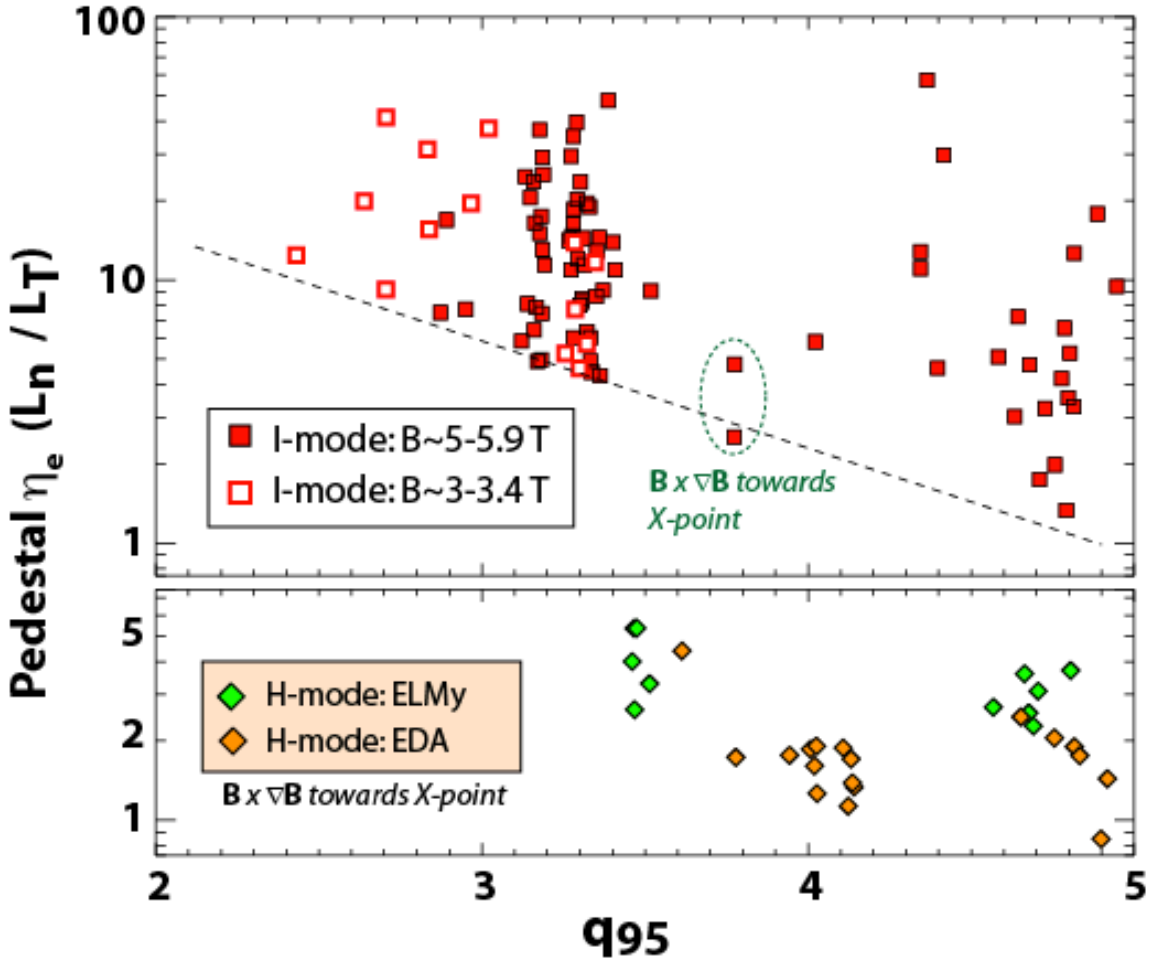
100
10
1
Pedestal η_e (L_n / L_T)
I-mode: B~5-5.9 T
I-mode: B~3-3.4 T
B x ∇B towards
X-point
5
2
1
H-mode: ELMy
H-mode: EDA
B x ∇B towards X-point
2
3
4
5
q95

Fig. 14

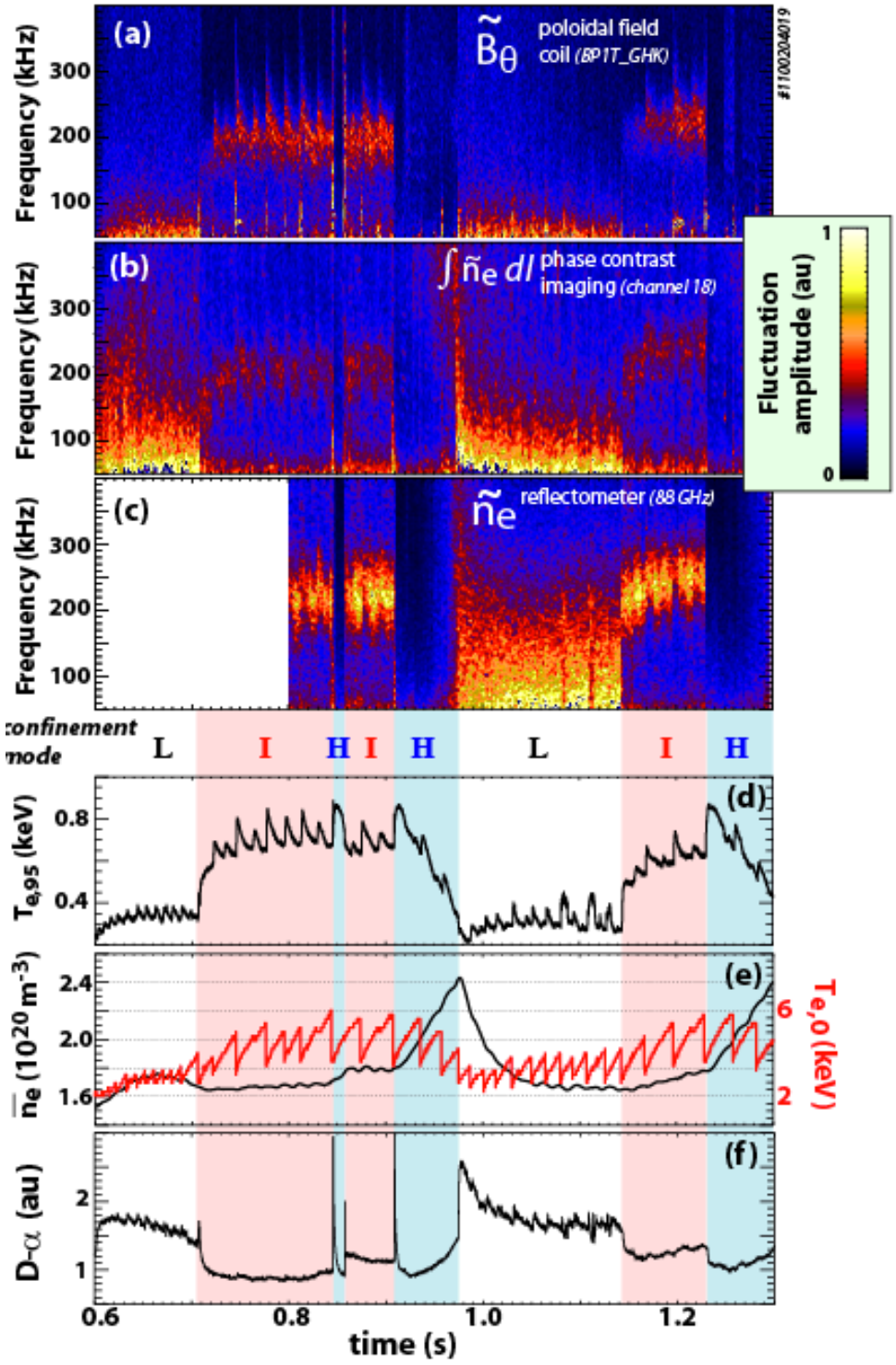
(a)
poloidal field coil (BP1T_GHK)
#1100204019
Frequency (kHz)
300
200
100
(b)
phase contrast imaging (channel 18)
Fluctuation amplitude (au)
1
0
(c)
reflectometer (88 GHz)
confinement mode
L
I
H
I
H
L
I
H
(d)
(e)
(f)
time (s)
0.6
0.8
1.0
1.2

Fig. 15

References

[1] Lawson, J.D., P Phys Soc Lond B **70** 6-10 (1957).

[2] Shimada, M., Campbell, D.J., Mukhovatov, V., Fujiwara, M., Kirneva, N., Lackner, K., et al., Nuclear Fusion **47** S1-S17 (2007).

[3] Jardin, S.C., Kessel, C.E., Mau, T.K., Miller, R.L., Najmabadi, F., Chan, V.S., et al., Fusion Engineering and Design **80** 25-62 (2006).

[4] Doyle, E.J., Houlberg, W.A., Kamada, Y., Mukhovatov, V., Osborne, T.H., Polevoi, A., et al., Nuclear Fusion **47** S18-S127 (2007).

[5] Greenwald, M., Boivin, R.L., Bombarda, F., Bonoli, P.T., Fiore, C.L., Garnier, D., et al., Nuclear Fusion **37** 793-807 (1997).

[6] Snyder, P.B., Wilson, H.R., Ferron, J.R., Lao, L.L., Leonard, A.W., Osborne, T.H., et al., Physics of Plasmas **9** 2037-43 (2002).

[7] Loarte, A., Lipschultz, B., Kukushkin, A.S., Matthews, G.F., Stangeby, P.C., Asakura, N., et al., Nuclear Fusion **47** 203-63 (2007).

[8] Marmar, E.S., CMod-group, Fusion Science and Technology **51** 261-5 (2007).

[9] Ryter, F., Suttrop, W., Brusehaber, B., Kaufmann, M., Mertens, V., Murmann, H., et al., Plasma Physics and Controlled Fusion **40** 725-9 (1998).

[10] Hubbard, A.E., Hughes, J.W., Bespamyatnov, I.O., Biewer, T., Cziegler, I., Labombard, B., et al., Physics of Plasmas **14** 056109 (2007).

[11] ASDEX-team, Nuclear Fusion **29** 1959-2040 (1989).

[12] Hubbard, A.E., Boivin, R.L., Draket, J.F., Greenwald, M., In, Y., Irby, J.H., et al., Plasma Physics and Controlled Fusion **40** 689-92 (1998).

[13] Carlstrom, T.N., Burrell, K.H., Groebner, R.J., Plasma Physics and Controlled Fusion **40** 669-72 (1998).

[14] Groebner, R.J., Carlstrom, T.N., Plasma Physics and Controlled Fusion **40** 673-7 (1998).

[15] McDermott, R.M., Lipschultz, B., Hughes, J.W., Catto, P.J., Hubbard, A.E., Hutchinson, I.H., et al., Physics of Plasmas **16** 056103 (12 pp.) (2009).

[16] Ongena, J., Messiaen, A.M., Van Wassenhove, G., Weynants, R.R., Borgermans, P., Dumortier, P., et al., "Overview of heating and improved confinement (I-mode) on TEXTOR with NBI and ICRH". Proceedings of the Fourteenth International Conference on Plasma Physics and Controlled Nuclear Fusion Research, 30 Sept-7 Oct 1992; 1992; Vienna, Austria.

[17] Bonoli, P.T., Parker, R., Wukitch, S.J., Lin, Y., Porkolab, M., Wright, J.C., et al., Fusion Science and Technology **51** 401-36 (2007).

[18] Carlstrom, T.N., Gohil, P., Watkins, J.G., Burrell, K.H., Coda, S., Doyle, E.J., et al., Plasma Physics and Controlled Fusion **36** A147-A52 (1994).

[19] Titus, P., Zaks, J., Vieira, R., Gwinn, D., Labombard, B., "C-MOD cryopump design and analysis". 21st IEEE/NPSS Symposium on Fusion Engineering SOFE 05 (IEEE Cat No05CH37764); 2007; Piscataway, NJ, USA.

[20] Terry, J.L., Cziegler, I., Hubbard, A.E., Snipes, J.A., Hughes, J.W., Greenwald, M.J., et al., Journal of Nuclear Materials **363-365** 994-9 (2007).

[21] Lipschultz, B., Lin, Y., Reinke, M.L., Hubbard, A., Hutchinson, I.H., Irby, J., et al., Physics of Plasmas **13** 56117-1 (2006).

[22] Greenwald, M., Boivin, R., Bonoli, P., Budny, R., Fiore, C., Goetz, J., et al., Physics of Plasmas **6** 1943-9 (1999).
[23] Basse, N.P., Dominguez, A., Edlund, E.M., Fiore, C.L., Granetz, R.S., Hubbard, A.E., et al., Fusion Science and Technology **51** 476-507 (2007).
[24] Lin, L., Edlund, E.M., Porkolab, M., Lin, Y., Wukitch, S.J., Review of Scientific Instruments **77** 10-918 (2006).
[25] Lin, Y., Irby, J., Stek, P., Hutchinson, I., Snipes, J., Nazikian, R., et al., Review of Scientific Instruments **70** 1078-81 (1999).
[26] Terry, J.L., Zweben, S.J., Umansky, M.V., Cziegler, I., Grulke, O., LaBombard, B., et al., Journal of Nuclear Materials **390-391** 339-42 (2009).
[27] McDermott, R. "Edge radial electric field studies via charge-exchange recombination spectroscopy on the Alcator C-Mod tokamak" [Ph.D. thesis]. Cambridge, MA: Massachusetts Institute of Technology; 2009.
[28] Wakatani, M., Mukhovatov, V.S., Burrell, K.H., Connor, J.W., Cordey, J.G., Esipchuk, Y.V., et al., Nuclear Fusion **39** 2175-249 (1999).
[29] Martin, Y.R., Takizuka, T., Journal of Physics: Conference Series **123** 012033-44 (2008).
[30] Greenwald, M., Basse, N., Bonoli, P., Bravenec, R., Edlund, E., Ernst, D., et al., Fusion Science and Technology **51** 266-87 (2007).
[31] Hughes, J.W., Hubbard, A.E., Mossessian, D.A., LaBombard, B., Biewer, T.M., Granetz, R.S., et al., Fusion Science and Technology **51** 317-41 (2007).
[32] Rice, J.E., Terry, J.L., Goetz, J.A., Wang, Y., Marmar, E.S., Greenwald, M., et al., Physics of Plasmas **4** 1605-9 (1997).
[33] Rice, J.E., Terry, J.L., Marmar, E.S., Granetz, R.S., Greenwald, M.J., Hubbard, A.E., et al., Fusion Science and Technology **51** 357-68 (2007).
[34] Howard, N., Greenwald, M., Rice, J.E., submitted to Rev Sci Instrum (2010).
[35] Rice, J.E., Bonoli, P.T., Goetz, J.A., Greenwald, M.J., Hutchinson, I.H., Marmar, E.S., et al., Nuclear Fusion **39** 1175-86 (1999).
[36] Groebner, R.J., Baker, D.R., Burrell, K.H., Carlstrom, T.N., Ferron, J.R., Gohil, P., et al., Nuclear Fusion **41** 1789-800 (2001).
[37] Hughes, J.W., Mossessian, D.A., Hubbard, A.E., LaBombard, B., Marmar, E.S., Physics of Plasmas **9** 3019-30 (2002).
[38] Loarte, A., Saibene, G., Sartori, R., Campbell, D., Becoulet, M., Horton, L., et al., Plasma Physics and Controlled Fusion **45** 1549-69 (2003).
[39] Hughes, J.W., LaBombard, B., Terry, J., Hubbard, A., Lipschultz, B., Nuclear Fusion **47** 1057-63 (2007).
[40] Neuhauser, J., Coster, D., Fahrbach, H.U., Fuchs, J.C., Haas, G., Herrmann, A., et al., Plasma Physics and Controlled Fusion **44** 855-69 (2002).
[41] Snyder, P.B., Hammett, G.W., Physics of Plasmas **8** 3199-216 (2001).
[42] LaBombard, B., Rice, J.E., Hubbard, A.E., Hughes, J.W., Greenwald, M., Granetz, R.S., et al., Physics of Plasmas **12** 56111-1 (2005).
[43] Rice, J.E., Hubbard, A.E., Hughes, J.W., Greenwald, M.J., LaBombard, B., Irby, J.H., et al., Nuclear Fusion **45** 251-7 (2005).